Atmos. Chem. Phys. Discuss., 14, 12819–12862, 2014
www.atmos-chem-phys-discuss.net/14/12819/2014/
doi:10.5194/acpd-14-12819-2014
© Author(s) 2014. CC Attribution 3.0 License.

Atmospheric Chemistry and Physics Discussions

This discussion paper is/has been under review for the journal Atmospheric Chemistry and Physics (ACP). Please refer to the corresponding final paper in ACP if available.

A regional CO_2 observing system simulation experiment for the ASCENDS Satellite Mission

J. S. Wang[1,2], S. R. Kawa[2], J. Eluszkiewicz[3], D. F. Baker[4], M. Mountain[3], J. Henderson[3], T. Nehrkorn[3], and T. S. Zaccheo[3]

[1]Universities Space Research Association, Columbia, MD, USA
[2]NASA Goddard Space Flight Center, Greenbelt, MD, USA
[3]Atmospheric and Environmental Research, Lexington, MA, USA
[4]Cooperative Institute for Research in the Atmosphere, Colorado State University, Fort Collins, CO, USA

Received: 19 February 2014 – Accepted: 24 April 2014 – Published: 20 May 2014

Correspondence to: J. S. Wang (james.s.wang@nasa.gov)

Published by Copernicus Publications on behalf of the European Geosciences Union.

Abstract

Top-down estimates of the spatiotemporal variations in emissions and uptake of CO_2 will benefit from the increasing measurement density brought by recent and future additions to the suite of in situ and remote CO_2 measurement platforms. In particular, the planned NASA Active Sensing of CO_2 Emissions over Nights, Days, and Seasons (ASCENDS) satellite mission will provide greater coverage in cloudy regions, at high latitudes, and at night than passive satellite systems, as well as high precision and accuracy. In a novel approach to quantifying the ability of satellite column measurements to constrain CO_2 fluxes, we use a portable library of footprints (surface influence functions) generated by the WRF-STILT Lagrangian transport model in a regional Bayesian synthesis inversion. The regional Lagrangian framework is well suited to make use of ASCENDS observations to constrain fluxes at high resolution, in this case at 1° latitude × 1° longitude and weekly for North America. We consider random measurement errors only, modeled as a function of mission and instrument design specifications along with realistic atmospheric and surface conditions. We find that the ASCENDS observations could potentially reduce flux uncertainties substantially at biome and finer scales. At the 1° × 1°, weekly scale, the largest uncertainty reductions, on the order of 50 %, occur where and when there is good coverage by observations with low measurement errors and the a priori uncertainties are large. Uncertainty reductions are smaller for a 1.57 µm candidate wavelength than for a 2.05 µm wavelength, and are smaller for the higher of the two measurement error levels that we consider (1.0 ppm vs. 0.5 ppm clear-sky error at Railroad Valley, Nevada). Uncertainty reductions at the annual, biome scale range from ∼ 40 % to ∼ 75 % across our four instrument design cases, and from ∼ 65 % to ∼ 85 % for the continent as a whole. Our uncertainty reductions at various scales are substantially smaller than those from a global ASCENDS inversion on a coarser grid, demonstrating how quantitative results can depend on inversion methodology. The a posteriori flux uncertainties we obtain, ranging from 0.01 to

ACPD
14, 12819–12862, 2014

0.06 Pg C yr^{-1} across the biomes, would meet requirements for improved understanding of long-term carbon sinks suggested by a previous study.

1 Introduction

Quantification of surface fluxes of CO_2 and other greenhouse gases (GHG) over a range of spatial and temporal scales is of critical importance for understanding the processes that drive source/sink variability and climate-biogeochemistry feedbacks. The need to monitor GHG fluxes also follows from climate policy initiatives such as the Kyoto Protocol and possible follow-on agreements, along with their implementation (e.g., emissions trading and treaty verification). While direct "bottom-up" (inventory) approaches are considered accurate to within 10 % in the annual mean for fossil fuel CO_2 emissions in North America (Gurney et al., 2009), "top-down" (inverse) methods are the tool of choice to infer CO_2 sources and sinks from the terrestrial biosphere and oceans on a range of scales (Peters et al., 2007). In the top-down approach, fluxes are inferred from atmospheric CO_2 measurements by means of an atmospheric transport model linking the measurements to fluxes upwind. The availability of abundant and accurate measurements and realistic transport models is key to the success of this approach (e.g. Enting et al., 1995). Consequently, large investments have been made in establishing reliable measurement networks, including in situ measurements of CO_2 concentrations from the surface, towers, and aircraft (e.g. the NOAA ESRL Carbon Cycle Cooperative Global Air Sampling Network (Dlugokencky et al., 2013), and the Earth Networks Greenhouse Gas Network, http://ghg.earthnetworks.com/), and satellite missions dedicated to measurement of CO_2 column amounts. The last include the Greenhouse gases Observing SATellite (GOSAT) launched in January 2009 (Yokota et al., 2009), the Orbiting Carbon Observatory 2 (OCO-2) to be launched in 2014 (Crisp et al., 2008; Eldering et al., 2012), and the planned Active Sensing of CO_2 Emissions over Nights, Days, and Seasons (ASCENDS) mission recommended by the US National Academy of Sciences Decadal Survey (NRC, 2007).

ACPD
14, 12819–12862, 2014

The objective of our study is to quantify the ability of ASCENDS column measurements to constrain CO_2 fluxes top-down at relatively high resolution. The ASCENDS active measurement concept offers unique capabilities compared with passive satellite systems that rely on thermal emission or reflected sunlight (Kawa et al., 2010). These capabilities will enhance spatial and temporal coverage while providing high precision and accuracy. ASCENDS will extend coverage through its ability to sample in small cloud gaps and through thin clouds without interference. In addition, since a lidar-based system does not require the presence of the sun, it allows for observations of high-latitude regions during winter. Measurements can be made both night and day, thereby reducing sampling bias due to (and potentially providing constraints on) diurnal variations in CO_2 fluxes driven by ecosystem respiration and primary production.

Global studies of the impact of satellite measurements on top-down estimates of CO_2 fluxes, beginning with the study of Rayner and O'Brien (2001), have established the benefit of using satellite measurements for constraining CO_2 fluxes at a precision level similar to or better than that provided by existing in situ networks. At present, these approaches estimate the reduction of flux uncertainties stemming from the availability of satellite data using an inverse solution for relatively coarse grid boxes or regions at weekly to monthly resolution (e.g. Houweling et al., 2004; Chevallier et al., 2007; Feng et al., 2009; Baker et al., 2010; Kaminski et al., 2010; Hungershoefer et al., 2010; Basu et al., 2013). The present study extends these global studies to the regional scale using simulated ASCENDS data. Regional trace gas inversions are well-suited for making use of high-density satellite observations to constrain fluxes at fine scales. Regional transport models are less computationally expensive to run than global transport models for a given resolution, so it is more tractable to run a regional model at high resolution. The more precise determination of source–receptor relationships allows one to solve for fluxes at a finer resolution. This reduces potential "aggregation error" resulting from assuming fixed fine-scale flux patterns when optimizing scaling factors on a coarser scale (Kaminski et al., 2001; Engelen et al., 2002; Gerbig et al., 2003).

ACPD
14, 12819–12862, 2014

We use a novel approach for our inversions that facilitates high-resolution evaluation of satellite column measurements. The approach relies on a Lagrangian (airmass-following) transport model, run backward in time from the observation points (receptors) using ensembles of particles, to generate footprints describing the sensitivity of satellite CO_2 measurements to surface fluxes in upwind regions. This approach enables more precise simulation of transport in the near field than running source pulses through an Eulerian (with fixed frame of reference) transport model, since, in the former, meteorological fields are interpolated to the subgrid-scale locations of particles. Thus, filamentation processes, for example, can be resolved (Lin et al., 2003), and representation errors (Pillai et al., 2010) are minimized. The Lagrangian approach, implemented in the backward (receptor-oriented) mode, offers a natural way of calculating the adjoint of the atmospheric transport model. The utility of Lagrangian particle dispersion models is well established for regional trace gas flux inversions involving in situ observations (e.g. Gerbig et al., 2003; Lin et al., 2004; Kort et al., 2008, 2010; Zhao et al., 2009; Schuh et al., 2010; Göckede et al., 2010a; Gourdji et al., 2012; Miller et al., 2012, 2013; McKain et al., 2012; Lauvaux et al., 2012). A convenient feature of Lagrangian footprints is their portability – they can be shared with other groups and readily applied to different flux models, inversion approaches, and molecular species, thus enabling comparisons based on a common modeling component. In addition, footprints for different measurement platforms can be merged easily in an inversion.

In this observing system simulation experiment (OSSE), we utilize the Stochastic Time-Inverted Lagrangian Transport (STILT) particle dispersion model (Lin et al., 2003) driven by meteorological fields from the Weather Research and Forecasting (WRF) model (Skamarock and Klemp, 2008) in a domain encompassing North America, in a Bayesian inversion. The WRF-STILT (Nehrkorn et al., 2010) footprints are used to compute weekly flux uncertainties over a 1° latitude × 1° longitude grid. This study focuses on land-based biospheric fluxes. We report results based on realistic sampling and observation errors for ASCENDS and other input data fields for year 2007. Section 2 provides details on our inputs and inversion methods, and presents examples of

ACPD
14, 12819–12862, 2014

observation uncertainties, a priori flux uncertainties, and WRF-STILT footprint maps. Section 3 presents posterior flux uncertainty results at various spatial and temporal scales, as well as comparisons with other studies, including preliminary results from a companion global ASCENDS OSSE. Section 4 discusses target and threshold requirements for instrument design parameters with respect to addressing key scientific questions. It also discusses additional sources of uncertainty and limitations of our analysis, as well as other considerations regarding ASCENDS. Section 5 contains concluding remarks.

2 Methods

2.1 Inversion approach

We use a Bayesian synthesis inversion method, which optimizes the agreement between model and observed CO_2 concentrations and a priori and a posteriori flux estimates in a least-squares manner (e.g. Enting et al., 1995). Since we focus on uncertainty levels in estimating the constraint on fluxes that ASCENDS observations will provide, we did not perform a full inversion and computed only the a posteriori flux error covariance associated with the inversion solution. The a posteriori flux error covariance matrix is given by

$$\hat{\mathbf{S}} = \left(\mathbf{K}^T \mathbf{S}_\varepsilon^{-1} \mathbf{K} + \mathbf{S}_a^{-1}\right)^{-1}, \quad (1)$$

where

K is the Jacobian matrix relating fluxes to concentrations
(**K*x*** = ***c***, where ***x*** is the vector of fluxes and ***c*** denotes concentrations)
$\mathbf{S}_\varepsilon$ is the observation error covariance matrix
$\mathbf{S}_a$ is the a priori flux error covariance matrix.

ACPD
14, 12819–12862, 2014

We directly solve for $\hat{\mathbf{S}}$, the square roots of the diagonal elements of which provide the estimates of the a posteriori flux uncertainties.

We solve for flux uncertainties in each land cell on a $1^\circ \times 1^\circ$ grid across North America (from 10° N to 70° N and from 170° W to 50° W). The time span is 5 weeks in each of the 4 seasons in 2007 (the first 4 weeks of January, April, July, and October plus the week preceding each of those months). We focus on weekly flux resolution in this study, rather than daily or higher resolution, for computational efficiency. In addition, the Decadal Survey called for a satellite mission that can constrain carbon cycle fluxes at weekly resolution on 1° grids (NRC, 2007). The ASCENDS observations would likely also provide significant constraints on fluxes at higher resolutions such as daily, as suggested by test inversions not reported here.

We solve Eq. (1) using the standard matrix inversion function in the Interactive Data Language (IDL) software package. We verified the solution using the alternative singular value decomposition approach (Rayner et al., 1999), again in IDL. Given the large dimensions of the matrices- more than 15 000 10 s average observations each month and 13 205 weekly flux elements over each 5 week period, the procedure requires large amounts of computer memory but a modest amount of processing time-several hours per monthly inversion on the NASA Center for Climate Simulation high-performance computing system.

2.2 Observational sampling and simulated measurement uncertainties

We consider candidate lidar wavelengths near 1.57 µm and 2.05 µm (Caron and Durand, 2009). These have peak sensitivities in the mid- and lower troposphere, respectively (Fig. 1). Other candidate wavelengths with different vertical sensitivities and error characteristics are possible and could be assessed with the same inversion methodology. We derive the temporal/spatial sampling and random error characteristics for ASCENDS pseudo-data based on real cloud/aerosol and surface backscatter conditions for year 2007 in a method similar to that of Kawa et al. (2010). Observation

ACPD
14, 12819–12862, 2014

locations are taken from Cloud-Aerosol Lidar and Infrared Pathfinder Satellite Observation (CALIPSO) satellite orbit tracks. We use only locations that fall within the domain used in the WRF runs (Sect. 2.4), excluding those within 400 km of the boundaries to provide adequate WRF coverage to simulate back trajectory calculations inside the domain (Fig. 2). The error calculations use CALIPSO optical depth (OD) data, together with surface backscatter calculated from Moderate Resolution Imaging Spectroradiometer (MODIS) satellite reflectance over land or glint backscatter, calculated using 10 m analyzed wind speeds (Hu et al., 2008) interpolated to the sample locations, over ocean. Samples with total column cloud plus aerosol OD > 0.7 are rejected. For each wavelength case, the measurement errors at each location are scaled to two possible performance levels: 0.5 ppm and 1.0 ppm error under clear-sky conditions (cloud/aerosol OD = 0) with reflectivity equal to that found at Railroad Valley (RRV), Nevada. The errors for each 5 km (0.74 s) individual CALIPSO observation point are aggregated over 10 s intervals to increase signal-to-noise for the pseudo-data, using the formula $\sigma(10\,\mathrm{s}) = \sqrt{\frac{\sum_{i=1}^{N} \sigma(5\,\mathrm{km})_i^2}{N^2}}$, where N is the number of valid 5 km observations across the 10 s span. Such a 10 s, conditionally-sampled measurement is expected to represent the basic ASCENDS CO_2 data granule. The uncertainties in the series of 10 s pseudo-data are assumed to be uncorrelated, i.e. the observation error covariance matrix $\mathbf{S}_\varepsilon$ is diagonal.

Examples of the coverage of ASCENDS observations available for analysis and their associated uncertainties (for a reference uncertainty at RRV of 0.5 ppm) are shown in Fig. 2 over seven-day periods in January and July for the two candidate wavelengths. ASCENDS provides dense coverage over the domain with few large gaps, especially in July. A large majority of the 10 s-average observations have uncertainties of < 2 ppm in all four cases except for 2.05 µm in January. The uncertainties are especially small over land areas, which is helpful for constraining terrestrial fluxes. The uncertainties are generally larger for 2.05 µm than for 1.57 µm (by a factor of 1–1.6 over snow-free

ACPD
14, 12819–12862, 2014

land and a factor of 1.6–1.8 over snow-/ice-covered areas) except in ice-free oceanic areas, where the uncertainties are similar (Fig. 2e and f).

2.3 A priori flux uncertainties

We derived a priori flux uncertainties at $1^{\circ} \times 1^{\circ}$ resolution from the variability of net ecosystem exchange (NEE) in the Carnegie–Ames–Stanford–Approach (CASA) biogeochemical model coupled to version 3 of the Global Fire Emissions Database (GFED3) (Randerson et al., 1996; van der Werf et al., 2006, 2010). In the version of CASA used here, a sink of $\sim 100\,\mathrm{Tg\,C\,yr^{-1}}$ is induced by crop harvest in the US Midwest that is prescribed based on National Agriculture Statistics Service data on crop area and harvest. We neglected uncertainties in fossil fuel emissions, assuming like most previous inversion studies that those emissions are relatively well known. We ignored oceanic fluxes as well for this study, since their uncertainties are also relatively small (e.g. Baker et al., 2010).

The a priori flux uncertainties were specifically derived from the standard deviations of daily mean CASA-GFED NEE over each month in 2007, divided by $\sqrt{7}$ to scale approximately to weekly uncertainties. This approach assumes that the more variable the model fluxes are in a particular grid cell and month, the larger the errors tend to be; the same reasoning has been applied in previous inversion studies to the estimation of model-data mismatch errors (e.g. Wang et al., 2008). We enlarged the resulting uncertainties uniformly by a factor of 4 to approximate the magnitude of those used in the global ASCENDS OSSE described in this paper; these are, in turn, essentially the same as the standard ones of Baker et al. (2010), based on differences between two sets of bottom-up flux estimates. In addition to allowing for better comparison of the two OSSEs, the enlargement by a factor of 4 is consistent with suggestions by biospheric model intercomparisons that the true flux uncertainty is greater than that based on a single model's variability (Huntzinger et al., 2012).

Off-diagonal elements of the a priori flux error covariance matrix are filled using spatial and temporal error correlations derived from an isotropic exponential decay model

ACPD
14, 12819–12862, 2014

with month-specific correlation lengths (Table 1) estimated from ground-based and aircraft CO_2 data in a North America regional inversion by Gourdji et al. (2012). Although these correlation lengths are not strictly applicable to our study, which has a different setup from that in the geostatistical inverse modeling system of Gourdji et al., they are nonetheless reasonable estimates in general for the purposes of this study. Note that Gourdji et al. used a 3 hourly flux resolution, so the temporal correlation lengths may be too short for the coarser weekly resolution of our study. Chevallier et al. (2012) show that aggregation of fluxes to coarser scales increases the error correlation length. The analysis by Chevallier et al. (2012) using global flux tower data found a weekly-scale temporal error correlation length of 36 days, longer than the values we use. They found a spatial correlation length of less than 100 km at the site scale (~ 1 km), increasing to 500 km at a 300 km-grid scale; our correlation lengths (100 km-grid) mostly fall within that range. In a test, we used alternative values for the spatiotemporal correlation lengths derived from the Chevallier et al. study, and found that the inversion results are moderately sensitive (Sect. 3.1).

Our CASA-GFED-based a priori flux uncertainties, scaled to approximate the values used by Baker et al. (2010), are shown in Fig. 3. The largest uncertainties occur generally where the absolute value of NEE is highest, e.g., in the "Corn Belt" of the US in summer. The spatial and seasonal variations exhibit similarities to those of Baker et al. (2010).

2.4 WRF-STILT Model, Footprints, and Jacobians

The STILT Lagrangian model, driven by WRF meteorological fields, has features, including a realistic treatment of convective fluxes and mass conservation properties, that are important for accurate top-down estimates of GHG fluxes that rely on small gradients in the measured concentrations (Nehrkorn et al., 2010). In the present application of STILT (www.stilt-model.org, revision 640), hourly output from WRF version 2.2 is used to provide the transport fields at a horizontal resolution of 40 km with 31 eta levels in the vertical, over a North American domain (Fig. 2a). Meteorological fields

ACPD
14, 12819–12862, 2014

from the North American Regional Reanalysis (NARR) at 32 km resolution are used to provide initial and boundary conditions for the WRF runs. To prevent drift of the WRF simulations from the analyses, the meteorological fields (horizontal winds, temperature, and water vapor at all levels) are nudged to the NARR analysis every 3 h with a 1 h relaxation time and are reinitialized every 24 h (at 00:00 UTC). Simulations are run out for 30 h, but only hours 7–30 from each simulation are used to avoid spin-up effects during the first 6 h. The WRF physics options used here are the same as those described by Nehrkorn et al. (2010).

A footprint quantitatively describes how much surface fluxes originating in upwind regions contribute to the total mixing ratio at a particular measurement location; it has units of mixing ratio per unit flux. This is to be distinguished from a satellite footprint, the area of earth reflecting the lidar signal. In the current application, footprints are computed for each 5 km simulated observation that passes the cloud/aerosol filter in January, April, July, and October 2007 at 3 h intervals back to 10 days prior to the observation time. Separate footprint maps have been computed for 15 receptor positions a.g.l. for the purpose of vertically convolving with the lidar weighting functions and producing one weighted-average footprint per measurement. (The receptors are spaced 1 km apart in the vertical from 0.5 to 14.5 km a.g.l.) This procedure results in ~ 90 000 footprint calculations per day, placing stringent demands on our computational approach. In this study, STILT simulates the release of an ensemble of 500 particles at each receptor in the column.

It is important to note that although a footprint is defined for each of the 15 vertical levels, the footprint expresses the sensitivity of the mixing ratio measured at the receptor point located at that vertical level to the surface fluxes upwind, not the fluxes upwind at the same level. So intuitively, the footprints defined for receptor points located at high altitudes (e.g. 12.5, 13.5, 14.5 km) are often zero, indicating that a receptor at that upper level is not influenced by surface fluxes inside the domain (within the 10 day span examined here). Conversely, receptor points located at the lowest

ACPD
14, 12819–12862, 2014

levels (e.g. 0.5, 1.5, 2.5 km) tend to have large footprints (with values of the order of 10^{-3} ppm (μmol m^{-2} s^{-1})$^{-1}$ or higher), being most influenced by nearby surface fluxes.

Figure 4 shows the vertically-weighted footprints of a selected column measurement location (in southern Canada) over 10 days for the 1.57 and 2.05 μm wavelengths. Non-zero footprints occur wherever air observed at the receptor site has been in contact with the surface within the past 10 days. Patterns of vertical and horizontal atmospheric motion explain the somewhat unexpected spatial patterns of the footprints in this particular example, with very high values occurring at a significant distance upwind of the receptor (in the vicinity of Texas and Oklahoma) as well as immediately upwind. Vertical mixing lifts the signature of surface fluxes to higher levels, so that it can be detected by receptors at multiple levels, resulting in a higher value for the vertically-convolved footprint, while slower winds in a particular area, such as Texas and Oklahoma, can result in a larger time-integrated impact of fluxes on the observation. The footprint values are larger for 2.05 μm due to the higher sensitivity of that measurement near the surface, as previously discussed.

To construct the Jacobians, **K**, that enter Eq. (1), we averaged the footprints of all the 5 km receptor locations within a given 10 s interval, including only the land cells. We arranged the averaged footprints in a two-dimensional Jacobian, running across flux time intervals and grid cells in one direction and across observations in the other. (The 3 h flux intervals associated with each transport run are defined relative to fixed UTC times and not relative to the observation times.) We then aggregated the Jacobian elements to the final flux resolution, e.g., weekly. For any particular month, we solved only for fluxes occurring in the week prior to the beginning of the month and in the first 4 weeks of that month.

Figure 5 shows the overall influence of the surface fluxes on the observations during each month (i.e. the average weekly Jacobian values for the 1.57 μm weighting function). Values tend to decrease from west to east, reflecting the general westerly wind direction, which transports CO_2 influences out of the domain more quickly for fluxes occurring closer to the eastern edge than for those farther west. Values also tend to

ACPD
14, 12819–12862, 2014

decrease towards the north and northwest and in the southernmost part of the continent: these areas lie close to the edges of the domain shown in Fig. 2a. Areas with smaller average footprint values are generally not as well constrained by the observations, as will be discussed later in this paper; thus, our domain boundaries artificially limit flux constraints in certain parts of the continent. Previous regional inversion studies may not have highlighted this issue because they used ground-based observations, whose sensitivities are more confined to near-field fluxes than those of satellite column measurements. We will quantify the impact of the boundaries on average footprint gradients in future work, providing guidance for future studies on optimal sizes and shapes of domains (e.g. shifted eastward) for avoiding large gradients while controlling computational cost.

Footprint values are largest in summer, again due to horizontal and vertical motions – winds during this season are relatively light and allow the fluxes to stay inside the domain for a long time, maximizing their integrated influence on observations in the domain, and vertical mixing across the deep boundary layer brings particles over a large portion of the column into contact with the surface.

Although WRF-STILT provides the capability to generate and optimize boundary condition influences on observed concentrations, this was not available at the time of this study and, consequently, we neglect uncertainties in the influence of boundary conditions in this analysis (discussed further in Sect. 4.2). Similarly, we neglect uncertainties due to the influence of North American fluxes occurring more than 10 days before a particular observation. Note that fluxes are often transported out of the domain within 10 days, so that these fluxes can only influence the observations via the boundary conditions.

3 Results

In the following, we present results for four cases involving different combinations of measurement wavelength and baseline error level: 1.57 µm and 0.5 ppm RRV error

ACPD
14, 12819–12862, 2014

(Case 1), 1.57 µm and 1.0 ppm (Case 2), 2.05 µm and 0.5 ppm (Case 3), and 2.05 µm and 1.0 ppm (Case 4).

3.1 A posteriori flux uncertainties at the grid level

A posteriori uncertainties (Fig. 6) are smaller than the a priori values (Fig. 3), an expected result of the incorporation of observational information. The reduction in uncertainty is often larger in areas that have higher a priori uncertainties, as can be seen more clearly in the maps of percentage reduction in uncertainty in Fig. 7. Uncertainty reductions are relatively large year-round in southern Mexico, adjacent parts of Central America, and the Pacific Northwest of the US; in April and October in the southeastern US; and in July in the US Midwest, southern Quebec, areas with forest fire emissions in central Canada (appearing as hot spots of uncertainty reduction), and Alaska and western Canada. A priori uncertainties are relatively high in these areas. The dependence of uncertainty reductions on the assumed priors can be understood thus: where a priori uncertainties are already small, observations are not able to provide a much tighter constraint, while in areas where a priori uncertainties are large, there is more room for observations to tighten the constraint.

The uncertainty reductions are not dependent simply on the prior uncertainties though. For example, the highest uncertainty reductions, up to 50 %, occur in southern Mexico in October, where a priori uncertainties are not especially large. The high uncertainty reductions here can be explained by the large Jacobian values (Fig. 5) combined with the low uncertainties of nearby observations (not shown). (Although a priori uncertainties and Jacobian values in July in this area are similar to those in October, observation uncertainties are higher, resulting in lower uncertainty reductions.) In general, uncertainty reductions tend to be higher where average Jacobian values are larger; observe the similarity of the spatial patterns in the January maps in Figs. 5a and 7a, for example. As described in Sect. 2.4, fluxes in western and central areas of the continent are captured by more observations in the domain than fluxes in the

ACPD
14, 12819–12862, 2014

east and close to the other edges; thus, the former can be better constrained in this inversion.

Another feature is that in July, the largest uncertainty reductions occur in northern Alaska and northwestern Canada, which have much smaller a priori uncertainties than places such as the Midwest. This is an effect of the smaller grid cells at higher latitudes: the a priori errors are correlated over larger numbers of cells at these latitudes given the spatially uniform correlation lengths we specify, so that the average flux over each cell is more tightly constrained than that for an otherwise comparable cell at lower latitudes. This is a less important issue when results are aggregated to the larger scales dealt with in later sections of this paper.

Uncertainty reductions are smallest in January, for several reasons: (1) a priori flux uncertainties are smallest during the dormant season, (2) observation errors are largest in winter due to the low reflectance of snow and ice cover at the measurement wavelengths, and (3) there is fast dispersion of fluxes in winter by strong winds, transporting fluxes out of the domain and out of detection by observations in the domain and thus reducing the average Jacobian values in January relative to the other months (Fig. 5). The ratio of the average of the Jacobian elements over the domain for January to that for July is 0.51 for the 1.57 µm wavelength.

Inversions for the 2.05 µm wavelength, with its higher sensitivity near the surface, result in greater uncertainty reduction, despite the larger observation errors over land (Fig. 8c vs. a, and d vs. b). Inversions assuming 1.0 ppm instead of 0.5 ppm error at RRV result in less uncertainty reduction (Fig. 8b vs. a, and d vs. c) as expected, with maximum uncertainty reduction of ∼ 30 % vs. ∼ 40 %, for 1.57 µm. These cases are compared further in the section below on biome-aggregated results.

The inversion results are sensitive to the assumed a priori error correlation lengths, with longer correlation lengths leading to more smooth uncertainty reduction patterns and larger uncertainty reductions. The reason for this is that longer a priori error correlation lengths result in fewer "unknowns" to be constrained by the observations. Rodgers (2000) shows that the inclusion of a priori correlations can result in more "degrees of

ACPD
14, 12819–12862, 2014

freedom for signal", i.e. more information provided by the measurements on the unknowns. We carried out a test with alternative values for the correlation lengths derived from the study by Chevallier et al. (2012) – a shorter spatial correlation length of 200 km and a longer temporal correlation length of 35 days, for all months. (We estimated these values from Fig. 5a and b of Chevallier et al. for the ∼ 100 km and 7 day aggregation of our inversion.) The resulting uncertainty reductions are smaller everywhere than those in our standard inversion at the grid scale, with values of up to 40 % in July and up to 15 % in January for Case 1 (compared to 45 % and 25 %, respectively, in the standard inversion). Apparently, the decrease in the spatial correlation length relative to the standard inversion has a larger effect than the increase in the temporal correlation length. We conclude that our inversion results vary moderately given two reasonable sets of estimates for the a priori spatiotemporal error correlation lengths.

3.2 Comparison with global inversion

We compare our regional OSSE results with those from a companion global OSSE to assess effects of methodological differences. The global OSSE uses the same ASCENDS dataset sampling and underlying observation error model as the regional OSSE. Among the primary differences are the global domain of the analysis and the coarser spatial resolution of the transport and flux solution, 4.5° latitude × 6° longitude. Other differences include the mathematical technique of the inversion (variational data assimilation, as in an earlier study, Baker et al., 2010), the Eulerian transport model, the spatial patterns of the a priori flux uncertainties (the overall magnitudes are not different, as described in Sect. 2.3), and the assumption of zero a priori correlation among fluxes (which can be justified by the coarser spatial scale). Comparison of our inversion results with results from the global study yields insight into the effect of inversion resolution on estimated flux uncertainties.

To aggregate our flux uncertainties to 4.5° × 6° resolution (in units of $\mu mol\,m^{-2}\,s^{-1}$) for comparison with the global inversion, we computed the variance of the average of the 1° × 1° land fluxes within each coarse grid cell, accounting for the error correlations

ACPD
14, 12819–12862, 2014

between the fine-scale cells and accounting for fractional overlap of some of the 1° × 1° cells with a 4.5° × 6° cell. Aggregating our a priori and a posteriori uncertainties in this manner, we find that our fractional uncertainty reductions over the 4 months are substantially smaller overall than those of the global inversion (Fig. 9). The differences in spatial distribution can be attributed in part to the different a priori uncertainty patterns. Reductions greater than 55 % cover large areas of North America in the global inversion, reaching values of over 75 %, whereas only a few 4.5° × 6° cells exhibit values greater than 55 % in the regional inversion. Note that we are not comparing exactly the same quantity, as the variational inversion method does not directly compute a full a posteriori error covariance matrix; rather, it uses (estimate – truth) statistics as a proxy for uncertainty, which is accurate for a sufficiently large sample (Baker et al., 2010). One possible reason for the difference in results is that information from the observations is used to optimize the fine-scale patterns in addition to the coarse-scale magnitudes in our inversion, in contrast to the global inversion in which a flat spatial distribution of flux is assumed inside each coarse grid box, providing an additional constraint on the fluxes. Thus, in our inversion, less information is available to reduce the uncertainties of the coarse-scale magnitudes, causing our uncertainty reductions to be smaller than those of the global inversion when compared at the same scale. (Note however that our imposing of a priori flux error correlations provides an additional constraint on fluxes and reduces the difference in effective flux resolution between the two studies.) On the other hand, the coarser global inversion is affected by larger aggregation errors (Kaminski et al., 2001; Engelen et al., 2002; Gerbig et al., 2003), which are not accounted for in the uncertainty reduction values. Another factor that likely contributes to the larger uncertainty reductions in the global inversion is that it allows fluxes to be constrained by observations both outside and inside a particular region. This can be especially important for fluxes close to the regional edges, as was discussed in Sect. 3.1. We do not attempt to quantify the individual impacts of the two main methodological differences or the various other differences.

ACPD
14, 12819–12862, 2014

3.3 Results aggregated to biomes and continent

For assessing large-scale changes in carbon sources and sinks, it is useful to aggregate high-resolution results to biomes and the entire continent, and to seasons and years. We use the biome definitions in Fig. 10 taken from Olson et al. (2001) with modifications by Gourdji et al. (2012). We used a similar approach for aggregating our results here to the one we used to aggregate results to a coarser grid (Sect. 3.2). In addition, we aggregated the global inversion results to the same biomes for comparison, summing the (estimate – truth) values and accounting for fractional biome coverage in each of the coarse grid cells.

Uncertainty reductions are largest in July and smallest in January, at the continental scale (Table 2). The uncertainty reductions for the 1.57 µm wavelength are on average 8 % smaller than those for 2.05 µm. The uncertainty reductions for the 1.57 µm wavelength with 0.5 ppm error are larger than those for 2.05 µm with 1.0 ppm error. The uncertainty reductions for 0.5 ppm error are on average 16 % larger than those for 1.0 ppm error. (Note that there is no reason to expect direct proportionality between measurement uncertainties and a posteriori flux uncertainties (Eq. 1), nor is there reason to expect proportionality between uncertainty reduction and a posteriori uncertainty.) The uncertainty reduction for the inversion with alternative a priori error correlation lengths, aggregated to the continent and month, is less than that for the standard inversion for all months except July, for which the uncertainty reduction is marginally larger. For July, the impact of the much longer temporal correlation length relative to the standard inversion on the aggregated result more than offsets that of the slightly shorter spatial correlation length. The annual uncertainty reduction for the alternative inversion is slightly larger than that for the standard inversion, because of the disproportionate influence of July, with its large a priori uncertainty.

At the annual, biome scale, our uncertainty reductions range from 50 % for the desert biome (averaged across the cases) to 70 % for the temperate grassland/shrubland biome (Fig. 11c). The reductions scale with increasing a priori uncertainty (Fig. 11a)

ACPD
14, 12819–12862, 2014

and observation quality and density, as before, and now also with biome area (Fig. 11d). We find a modest correlation between uncertainty reduction and area in the set of biomes here, with a linear correlation coefficient of 0.5. In addition, the uncertainty reduction is higher on the continental scale than on the biome scale. The a posteriori uncertainty increases with increasing area more slowly than does the a priori uncertainty since many of the a posteriori error covariance terms that are summed in the aggregation to biome are negative, whereas all of the a priori error covariance terms are positive or zero. This explains why uncertainty reduction tends to increase with increasing area.

Our a posteriori uncertainties range from 0.12 to 0.33 Pg C yr^{-1} at the monthly, continental scale across all four cases (Table 2), from 0.04 to 0.08 Pg C yr^{-1} at the annual, continental scale (Fig. 11a), and from 0.01 to 0.06 Pg C yr^{-1} at the annual, biome scale (Fig. 11a). To put these numbers into perspective, the estimated current global terrestrial sink is roughly 2.5 Pg C yr^{-1} (Le Quéré et al., 2012). Our uncertainties are generally similar to those from the North American regional inversion of Gourdji et al. (2012) (Fig. 11a) and the global inversion (Fig. 11b), a notable exception being the overall continental result of Gourdji et al. Gourdji et al. used a set of ground-based and aircraft measurements and a geostatistical inverse model to solve for biospheric fluxes and their uncertainties at a 1° × 1°, 3 hourly resolution in 2004. Our a posteriori uncertainty for N. America is small compared to Gourdji et al., likely because of the greater spatial coverage of ASCENDS as compared to the in situ network; some of the biomes are not well constrained by the in situ network (i.e. the ones for which Gourdji et al. did not report aggregated results). Note that the comparison is not a precise one, given the methodological differences. The global inversion's method for estimating uncertainties based on (estimate – truth) statistics cannot provide an annual uncertainty estimate for the one-year inversion and produces somewhat noisy results for individual months. Therefore, to compare the regional and global inversions, we took the RMS of the four monthly uncertainties. Our uncertainty reduction is smaller than that of the global inversion across all biomes for Case 1 (Fig. 11c), despite the prior uncertainties being

ACPD
14, 12819–12862, 2014

of similar magnitude on average (Fig. 11b). However, the continent-level uncertainty reductions are similar, at 78 % and 83 %, respectively, suggesting that there are larger negative correlations in the posterior errors among biomes in our analysis.

4 Discussion

4.1 Target and threshold requirements

We now discuss the implications of our analysis for the ASCENDS design. Hungershoefer et al. (2010) suggested levels of posterior flux uncertainty on different spatiotemporal scales that global CO_2 measurement missions should strive for to allow for answering key carbon cycle science questions. In the following, we evaluate our results relative to those requirements, the only such specific guidelines for CO_2 satellite missions in the scientific literature.

Hungershoefer et al. suggested that to determine where the global terrestrial C sink is occurring and whether C cycle feedbacks are occurring requires annual net carbon flux estimates with a precision better than 0.1 Pg C yr^{-1} (threshold) or 0.02 Pg C yr^{-1} (target) at a scale of 2000 km × 2000 km, similar to the biomes we consider. These precision levels are based on the range of estimated fluxes across various biomes. The proposed A-SCOPE active CO_2 measurement mission defined a similar target requirement – 0.02 Pg C yr^{-1} at a scale of 1000 km × 1000 km (Ingmann et al., 2008). According to our results (Fig. 11a), all tested ASCENDS cases would meet the minimum threshold requirement across all biomes easily, with a posteriori uncertainties ranging from 0.01 to 0.06 Pg C yr^{-1}. In addition, the two cases with 0.5 ppm error would meet the more stringent target requirement for a majority of biomes, while the two cases with 1.0 ppm error would meet it for 3 out of 7 biomes. The meeting of the target requirement is a consequence of the information provided by the observations and not merely an effect of the specified a priori uncertainty, given that the a priori uncertainty is higher than

ACPD
14, 12819–12862, 2014

the target level for all of the biomes with the exception of desert, the prior uncertainty for which is already at the target level.

4.2 Boundary condition uncertainties

A simplifying assumption in this analysis is the neglect of uncertainties in the boundary conditions (b.c.). It is especially important in a regional inversion (Eulerian or Lagrangian) to accurately account for the influence of lateral boundary inflow on concentrations within the domain (Göckede et al., 2010b; Lauvaux et al., 2012; Gourdji et al., 2012). Because we neglect b.c. uncertainties, we essentially assume that all of the information in the ASCENDS observations can be applied to reducing regional flux uncertainties rather than the combination of b.c. and flux uncertainties. Thus, the amount of flux uncertainty reduction reported here is likely higher than it would be if we accounted for b.c. uncertainties.

The magnitude of b.c. errors can be substantial. In addition to containing random errors, b.c. can also be a source of systematic errors. For example, Gourdji et al. (2012) found that two plausible sets of b.c. around North America generated inferred fluxes that differed by 0.7–0.9 Pg C yr^{-1} on the annual, continental scale (which is a very large amount compared to the annual a posteriori uncertainties for North America of 0.04–0.08 Pg C yr^{-1} that we estimated in our OSSE, Fig. 11a). They concluded that b.c. errors may be the primary control on flux errors at this coarse scale, while other factors such as flux resolution, priors, and model transport are more important at sub-domain scales.

Sparseness of observations has been a major cause of uncertainty in the boundary influence in previous regional inversions. Lauvaux et al. (2012), who conducted mesoscale inversions for the US Midwest using tower measurements, found b.c. errors to be a significant source of uncertainty in the C budget over 7 months. They estimated that a potential bias of 0.55 ppm in their b.c. translates into a flux error of 24 Tg C over 7 months in their 1000 km × 1000 km domain. Although they applied corrections to the model-derived b.c. using weekly aircraft profiles at four locations near

ACPD
14, 12819–12862, 2014

their domain boundaries, they stated that the b.c. uncertainties were still large given the limited duration (a few hours per week) and spatial extent of the airborne observations, and concluded that additional observations would be necessary to reduce the uncertainties. ASCENDS is promising in this respect, as it (along with other satellites) will provide more frequent and widespread observations of concentrations at regional boundaries, possibly lowering the role of b.c. in the overall C budget uncertainty to a minor one. ASCENDS observations could specifically be used in a global CO_2 data assimilation system to provide accurate b.c. for the regional flux inversion.

4.3 Other sources of error

This analysis did not evaluate the impact of potential systematic errors (biases) in the observations or the transport model, which are not well represented by the Gaussian errors assumed in traditional linear error analysis (Baker et al., 2010). Chevallier et al. (2007) demonstrated that potential biases in OCO satellite CO_2 measurements related to the presence of aerosols can completely negate the improvements to prior uncertainties provided by the measurements for the most polluted land regions and for ocean regions. In another OCO OSSE, Baker et al. (2010) found that a combination of systematic errors from aerosols, model transport, and incorrectly-assumed statistics could degrade both the magnitude and spatial extent of uncertainty improvements by about a factor of two over land, and even more over the ocean. Thus, it will be important to control systematic errors in ASCENDS observations and the transport model as well as minimizing random errors. Note that systematic observation errors can be expected to decrease over the course of the mission as adjustments are made to the measurement system and to the retrieval algorithms in calibration/validation activities.

4.4 Other considerations in evaluating ASCENDS

The potential combined use of multiple wavelengths in the ASCENDS measurements, e.g., various offsets from 1.57 µm, could provide additional information on surface

ACPD
14, 12819–12862, 2014

fluxes given the sensitivities to concentrations at different levels of the atmosphere. Furthermore, other CO_2 datasets will certainly be available alongside the ASCENDS data (e.g. from in situ networks), and the combination of datasets will provide stronger constraints on fluxes than any individual dataset (Hungershoefer et al., 2010).

Our comparison of the results for the 1.57 and 2.05 µm wavelengths over North America may be less applicable to other parts of the world. The global OSSE study by Hungershoefer et al. (2010), which compared various observing systems, including a satellite lidar system similar to ASCENDS, A-SCOPE, found that the 1.6 µm wavelength results in larger uncertainty reductions over South America while performing less well than 2.0 µm over temperate and cold regions. They attribute the better performance of 1.6 µm over South America to the strong vertical mixing of air there, which lessens the disadvantage of that wavelength's having weaker sensitivity to the lower troposphere. (However, they used a simpler error formulation.) On the other hand, in our global inversion, 2.05 µm results in larger uncertainty reductions than 1.57 µm throughout the world, by 8 % on average (for RRV error of 0.5–1.0 ppm).

5 Conclusions

We have conducted an observing system simulation for North America, using projected ASCENDS observation uncertainty estimates and a novel approach utilizing a portable footprint library generated from a high-resolution Lagrangian transport model, to quantify the surface CO_2 flux constraints provided by the future observations. We consider four possible configurations for the active optical remote sensing instrument covering two weighting functions and two random error levels. We find that the ASCENDS observations potentially reduce flux uncertainties substantially at fine and biome scales. At the 1° × 1° grid scale, weekly uncertainty reductions up to 30–45 % (averaged over the year) are achieved depending on the presumed instrument configuration. Relatively large uncertainty reductions occur year-round in southern Mexico and the US Pacific Northwest and seasonally in the southeastern and mid-western US and parts

ACPD
14, 12819–12862, 2014

of Canada and Alaska, when and where there is good coverage by observations with low uncertainties and a priori uncertainties are large. Uncertainty reductions at the annual, biome scale range from ∼ 40 % to ∼ 75 % across the four experimental cases, and from ∼ 65 % to ∼ 85 % for the continent as a whole. The uncertainty reductions for the 1.57 µm candidate wavelength are on average 10 % smaller than those for 2.05 µm across the biomes, and for 0.5 ppm RRV reference error are on average ∼ 25 % larger than those for 1.0 ppm error.

Our uncertainty reductions are substantially smaller than those of a global ASCENDS inversion at the 4.5° × 6° scale of the latter's model grid and at the biome scale. The global inversion benefits from the use of observations located around the world rather than in a limited region, and it has fewer unknowns to be solved for within North America. On the other hand, inversions at higher resolution enable investigation of biospheric and other processes at the finer scales that are needed to understand the mechanisms for inferred CO_2 flux variability and trends. In addition, by reducing aggregation error, higher-resolution inversions can produce flux estimates with less systematic error than those of lower-resolution inversions when aggregated to the same scale.

Based on the flux precision on an annual, biome scale suggested by Hungershoefer et al. (2010) for understanding the global carbon sink and feedbacks, ASCENDS observations would meet a threshold requirement for all biomes within the range of measurement designs considered here. The observations constrain a posteriori uncertainties to a level of 0.01–0.06 Pg C yr^{-1}, and could thus help pin down the location and magnitude of long-term C sinks. With regards to the more stringent target requirement, a subset of the instrument designs would meet the target for a majority of biomes.

The results we have presented may be optimistic, as uncertainties in boundary conditions and potential systematic errors in the observations and transport model that we have neglected would degrade the flux estimates. On the other hand, modifications to the size and location of our regional domain, e.g. an eastward shift, could improve the constraints by satellite observations on North American fluxes.

ACPD
14, 12819–12862, 2014

In future work, inversions in various regions (including, for example, South America) with a more comprehensive treatment of error sources could more definitively establish the usefulness of ASCENDS observations for constraining fluxes at fine and large scales and answering global carbon cycle science questions.

Acknowledgements. Work at NASA and AER has been supported by the NASA Atmospheric CO_2 Observations from Space program element and NASA ASCENDS Pre-Phase A activity funding. We are grateful to the NASA Ames HEC facility staff for assistance in executing the WRF-STILT runs on the Pleiades supercomputer, and to the NASA HEC Program for granting use of the Dali system at the NASA Center for Climate Simulation. We also thank J. Abshire, E. Browell, and R. Menzies for contributions to ASCENDS data characterization, G. J. Collatz for making available the CASA-GFED fluxes that we used to construct the a priori uncertainties, R. Aschbrenner for help with the footprint calculations, S. Gourdji for providing correlation parameters and the biome map, P. Rayner and A. Michalak for advice on inversions, M. Manyin and Y. Liu for computing help, L. Ott for help with transferring WRF-STILT files, and G. J. Collatz and E. McGrath-Spangler for comments on the manuscript.

References

Baker, D. F., Bösch, H., Doney, S. C., O'Brien, D., and Schimel, D. S.: Carbon source/sink information provided by column CO_2 measurements from the Orbiting Carbon Observatory, Atmos. Chem. Phys., 10, 4145–4165, doi:10.5194/acp-10-4145-2010, 2010.

Basu, S., Guerlet, S., Butz, A., Houweling, S., Hasekamp, O., Aben, I., Krummel, P., Steele, P., Langenfelds, R., Torn, M., Biraud, S., Stephens, B., Andrews, A., and Worthy, D.: Global CO_2 fluxes estimated from GOSAT retrievals of total column CO_2, Atmos. Chem. Phys., 13, 8695–8717, doi:10.5194/acp-13-8695-2013, 2013.

Butler, M. P., Davis, K. J., Denning, A. S., and Kawa, S. R.: Using continental observations in global atmospheric inversions of CO_2: North American carbon sources and sinks, Tellus B, 62, 550–572, doi:10.1111/j.1600-0889.2010.00501.x, 2010.

Caron, J. and Durand, Y.: Operating wavelengths optimization for a spaceborne lidar measuring atmospheric CO_2, Appl. Optics, 48, 5413–5422, 2009.

ACPD
14, 12819–12862, 2014

Chevallier, F., Bréon, F.-M., and Rayner, P. J.: Contribution of the Orbiting Carbon Observatory to the estimation of CO_2 sources and sinks: theoretical study in a variational data assimilation framework, J. Geophys. Res., 112, D09307, doi:10.1029/2006JD007375, 2007.

Crisp, D., Miller, C. E., and DeCola, P. L.: NASA Orbiting Carbon Observatory: measuring the column averaged carbon dioxide mole fraction from space, J. Appl. Remote Sens., 2, 023508, doi:10.1117/1.2898457, 2008.

Dlugokencky, E. J., Lang, P. M., Masarie, K. A., Crotwell, A. M., and Crotwell, M. J.: Atmospheric Carbon Dioxide Dry Air Mole Fractions from the NOAA ESRL Carbon Cycle Cooperative Global Air Sampling Network, 1968–2012, Version: 2013-08-28, available at: ftp://aftp.cmdl.noaa.gov/data/trace_gases/co2/flask/surface/ (last access: 18 February 2014), 2013.

Eldering, A., Solish, B., Kahn, P., Boland, S., Crisp, D., and Gunson, M.: High precision atmospheric CO_2 measurements from space: the design and implementation of OCO_2, IEEE Aerospace Conference Proceedings, 1805–1814, 2012.

Engelen, R. J., Denning, A. S., and Gurney, K. R.: On error estimation in atmospheric CO_2 inversions, J. Geophys. Res., 107, 4635, doi:10.1029/2002JD002195, 2002.

Enting, I. G., Trudinger, C. M., and Francey, R. J.: A synthesis inversion of the concentration and $\delta^{13}C$ of atmospheric CO_2, Tellus B, 47, 35–52, 1995.

Feng, L., Palmer, P. I., Bösch, H., and Dance, S.: Estimating surface CO_2 fluxes from space-borne CO_2 dry air mole fraction observations using an ensemble Kalman Filter, Atmos. Chem. Phys., 9, 2619–2633, doi:10.5194/acp-9-2619-2009, 2009.

Gerbig, C., Lin, J. C., Wofsy, S. C., Daube, B. C., Andrews, A. E., Stephens, B. B., Bakwin, P. S., and Grainger, C. A.: Towards constraining regional scale fluxes of CO_2 with atmospheric observations over a continent: 2. Analysis of COBRA data using a receptor-oriented framework, J. Geophys. Res., 108, 4757, doi:10.1029/2003JD003770, 2003.

Göckede, M., Michalak, A. M., Vickers, D., Turner, D. P., and Law, B. E.: Atmospheric inverse modeling to constrain regional scale CO_2 budgets at high spatial and temporal resolution, J. Geophys. Res., 115, D15113, doi:10.1029/2009JD012257, 2010a.

Göckede, M., Turner, D. P., Michalak, A. M., Vickers, D., and Law, B. E.: Sensitivity of a subregional scale atmospheric inverse CO_2 modeling framework to boundary conditions, J. Geophys. Res., 115, D24112, doi:10.1029/2010JD014443, 2010b.

Gourdji, S. M., Mueller, K. L., Yadav, V., Huntzinger, D. N., Andrews, A. E., Trudeau, M., Petron, G., Nehrkorn, T., Eluszkiewicz, J., Henderson, J., Wen, D., Lin, J., Fischer, M., Sweeney, C., and Michalak, A. M.: North American CO_2 exchange: inter-comparison of

ACPD
14, 12819–12862, 2014

modeled estimates with results from a fine-scale atmospheric inversion, Biogeosciences, 9, 457–475, doi:10.5194/bg-9-457-2012, 2012.
Gurney, K. R., Mendoza, D. L., Zhou, Y., Fischer, M. L., Miller, C. C., Geethakumar, S., and de la Rue du Can, S.: High resolution fossil fuel combustion CO_2 emission fluxes for the United States, Environ. Sci. Technol., 43, 5535–5541, doi:10.1021/es900806c, 2009.
Houweling, S., Breon, F.-M., Aben, I., Rödenbeck, C., Gloor, M., Heimann, M., and Ciais, P.: Inverse modeling of CO_2 sources and sinks using satellite data: a synthetic inter-comparison of measurement techniques and their performance as a function of space and time, Atmos. Chem. Phys., 4, 523–538, doi:10.5194/acp-4-523-2004, 2004.
Hungershoefer, K., Breon, F.-M., Peylin, P., Chevallier, F., Rayner, P., Klonecki, A., Houweling, S., and Marshall, J.: Evaluation of various observing systems for the global monitoring of CO_2 surface fluxes, Atmos. Chem. Phys., 10, 10503–10520, doi:10.5194/acp-10-10503-2010, 2010.
Huntzinger, D. N., Post, W. M., Wei, Y., Michalak, A. M., West, T. O., Jacobson, A. R., Baker, I. T., Chen, J. M., Davis, K. J., Hayes, D. J., Hoffman, F. M., Jain, A. K., Liu, S., McGuire, A. D., Neilson, R. P., Potter, C., Poulter, B., Price, D., Raczka, B. M., Tian, H. Q., Thornton, P., Tomelleri, E., Viovy, N., Xiao, J., Yuan, W., Zeng, N., Zhao, M., and Cook, R.: North American Carbon Program (NACP) regional interim synthesis: terrestrial biospheric model intercomparison, Ecol. Model., 232, 144–157, doi:10.1016/j.ecolmodel.2012.02.004, 2012.
Hu, Y., Stamnes, K., Vaughan, M., Pelon, J., Weimer, C., Wu, D., Cisewski, M., Sun, W., Yang, P., Lin, B., Omar, A., Flittner, D., Hostetler, C., Trepte, C., Winker, D., Gibson, G., and Santa-Maria, M.: Sea surface wind speed estimation from space-based lidar measurements, Atmos. Chem. Phys., 8, 3593–3601, doi:10.5194/acp-8-3593-2008, 2008.
Ingmann, P.: A-SCOPE, Advanced Space Carbon and Climate Observation of Planet Earth, Report for Assessment, SP-1313/1, ESA Communication Production Office, Noordwijk, the Netherlands, 2008.
Kaminski, T., Rayner, P., Heimann, M., and Enting, I.: On aggregation errors in atmospheric transport inversions, J. Geophys. Res., 106, 4703–4715, 2001.
Kaminski, T., Scholze, M., and Houweling, S.: Quantifying the benefit of A-SCOPE data for reducing uncertainties in terrestrial carbon fluxes in CCDAS, Tellus B, 62, 784–796, 2010.
Kawa, S. R., Erickson III, D. J., Pawson, S., and Zhu, Z.: Global CO_2 transport simulations using meteorological data from the NASA data assimilation system, J. Geophys. Res., 109, D18312, doi:10.1029/2004JD004554, 2004.

ACPD
14, 12819–12862, 2014

Kawa, S. R., Mao, J., Abshire, J. B., Collatz, G. J., Sun, X., and Weaver, C. J.: Simulation studies for a space-based CO_2 lidar mission, Tellus B, 62, 759–769, doi:10.1111/j.1600-0889.2010.00486.x, 2010.

Kort, E. A., Eluszkiewicz, J., Stephens, B. B., Miller, J. B., Gerbig, C., Nehrkorn, T., Daube, B. C., Kaplan, J. O., Houweling, S., and Wofsy, S. C.: Emissions of CH_4 and N_2O over the United States and Canada based on a receptor-oriented modeling framework and COBRA-NA atmospheric observations, Geophys. Res. Lett., 35, L18808, doi:10.1029/2008GL034031, 2008.

Kort, E. A., Andrews, A. E., Dlugokencky, E., Sweeney, C., Hirsch, A., Eluszkiewicz, J., Nehrkorn, T., Michalak, A., Stephens, B., Gerbig, C., Miller, J. B., Kaplan, J., Houweling, S., Daube, B. C., Tans, P., and Wofsy, S. C.: Atmospheric constraints on 2004 emissions of methane and nitrous oxide in North America from atmospheric measurements and receptor-oriented modeling framework, J. Integr. Environ. Sci., 7, 125–133, 2010.

Lauvaux, T., Schuh, A. E., Uliasz, M., Richardson, S., Miles, N., Andrews, A. E., Sweeney, C., Diaz, L. I., Martins, D., Shepson, P. B., and Davis, K. J.: Constraining the CO_2 budget of the corn belt: exploring uncertainties from the assumptions in a mesoscale inverse system, Atmos. Chem. Phys., 12, 337–354, doi:10.5194/acp-12-337-2012, 2012.

Le Quéré, C., Andres, R. J., Boden, T., Conway, T., Houghton, R. A., House, J. I., Marland, G., Peters, G. P., van der Werf, G. R., Ahlström, A., Andrew, R. M., Bopp, L., Canadell, J. G., Ciais, P., Doney, S. C., Enright, C., Friedlingstein, P., Huntingford, C., Jain, A. K., Jourdain, C., Kato, E., Keeling, R. F., Klein Goldewijk, K., Levis, S., Levy, P., Lomas, M., Poulter, B., Raupach, M. R., Schwinger, J., Sitch, S., Stocker, B. D., Viovy, N., Zaehle, S., and Zeng, N.: The global carbon budget 1959–2011, Earth Syst. Sci. Data, 5, 165–185, doi:10.5194/essd-5-165-2013, 2013.

Lin, J. C., Gerbig, C., Wofsy, S. C., Daube, B. C., Andrews, A. E., Davis, K. J., and Grainger, C. A.: A near-field tool for simulating the upstream influence of atmospheric observations: the Stochastic Time-Inverted Lagrangian Transport (STILT) model, J. Geophys. Res., 108, 4493, doi:10.1029/2002JD003161, 2003.

Mahadevan, P., Wofsy, S. C., Matross, D. M., Xiao, X., Dunn, A. L., Lin, J. C., Gerbig, C., Munger, J. W., Chow, V. Y., and Gottlieb, E. W.: A satellite-based biosphere parameterization for net ecosystem CO_2 exchange: vegetation Photosynthesis and Respiration Model (VPRM), Global Biogeochem. Cy., 22, GB2005, doi:10.1029/2006GB002735, 2008.

ACPD
14, 12819–12862, 2014

Matross, D. M.: Regional Scale Land-Atmosphere Carbon-Dioxide Exchange: Data Design and Inversion within a Receptor Oriented Modeling Framework, Ph.D. Thesis, Department of Earth and Planetary Sciences, Harvard University, Cambridge, Massachusetts, USA, 171 pp., 2006.

McKain, K., Wofsy, S. C., Nehrkorn, T., Eluszkiewicz, J., Ehleringer, J. R., and Stephens, B. B.: Assessment of ground-based atmospheric observations for verification of greenhouse gas emissions from an urban region, P. Natl. Acad. Sci. USA, 109, 8423–8428, 2012.

Miller, S. M., Kort, E. A., Hirsch, A. I., Dlugokencky, E. J., Andrews, A. E., Xu, X., Tian, H., Nehrkorn, T., Eluszkiewicz, J., Michalak, A. M., and Wofsy, S. C.: Regional sources of nitrous oxide over the United States: seasonal variation and spatial distribution, J. Geophys. Res., 117, D06310, doi:10.1029/2011JD016951, 2012.

Miller, S. M., Wofsy, S. C., Michalak, A. M., Kort, E. A., Andrews, A. E., Biraud, S. C., Dlugokencky, E. J., Eluszkiewicz, J., Fischer, M. L., Janssens-Maenhout, G., Miller, B. R., Miller, J. B., Montzka, S. A., Nehrkorn, T., and Sweeney, C.: Anthropogenic emissions of methane in the United States, P. Natl. Acad. Sci. USA, 110, 20018–20022, doi:10.1073/pnas.1314392110, 2013.

National Research Council: Earth Science and Applications from Space: National Imperatives for the Next Decade and Beyond, The National Academies Press, Washington, DC, 2007.

Nehrkorn, T., Eluszkiewicz, J., Wofsy, S. C., Lin, J. C., Gerbig, C., Longo, M., and Freitas, S.: Coupled Weather Research and Forecasting/Stochastic Time-Inverted Lagrangian Transport (WRF-STILT) model, Meteorol. Atmos. Phys., 107, 51–64, doi:10.1007/s00703-010-0068-x, 2010.

Olson, D. M., Dinerstein, E., Wikramanayake, E. D., Burgess, N. D., Powell, G. V. N., Underwood, E. C., D'Amico, J. A., Itoua, I., Strand, H. E., Morrison, J. C., Loucks, C. J., Allnutt, T. F., Ricketts, T. H., Kura, Y., Lamoreux, J. F., Wettengel, W. W., Hedao, P., and Kassem, K. R.: Terrestrial ecoregions of the world: a new map of life on earth, Bioscience, 51, 933–938, 2001.

Peters, W., Jacobson, A. R., Sweeney, C., Andrews, A. E., Conway, T. J., Masarie, K., Miller, J. B., Bruhwiler, L. M. P., Petron, G., Hirsch, A. I., Worthy, D. E. J., van der Werf, G. R., Randerson, J. T., Wennberg, P. O., Krol, M. C., and Tans, P. P.: An atmospheric perspective on North American carbon dioxide exchange: carbon Tracker, P. Natl. Acad. Sci. USA, 104, 18925–18930, 2007.

ACPD
14, 12819–12862, 2014

Pillai, D., Gerbig, C., Marshall, J., Ahmadov, R., Kretschmer, R., Koch, T., and Karstens, U.: High resolution modeling of CO_2 over Europe: implications for representation errors of satellite retrievals, Atmos. Chem. Phys., 10, 83–94, doi:10.5194/acp-10-83-2010, 2010.

Randerson, J. T., Thompson, M. V., and Malmstrom, C. M.: Substrate limitations for heterotrophs: implications for models that estimate the seasonal cycle of atmospheric CO_2, Global Biogeochem. Cy., 10, 585–602, 1996.

Rayner, P. J. and O'Brien, D. M.: The utility of remotely sensed CO_2 concentration data in surface source inversions, Geophys. Res. Lett., 28, 175–178, 2001.

Rayner, P. J., Enting, I. G., Francey, R. J., and Langenfelds, R.: Reconstructing the recent carbon cycle from atmospheric CO_2, $\delta^{13}C$ and O_2/N_2 observations, Tellus B, 51, 213–232, 1999.

Rienecker, M. M., Suarez, M. J., Gelaro, R., Todling, R., Bacmeister, J., Liu, E., Bosilovich, M. G., Schubert, S. D., Takacs, L., Kim, G.-K., Bloom, S., Chen, J., Collins, D., Conaty, A., Da Silva, A., Gu, W., Joiner, J., Koster, R. D., Lucchesi, R., Molod, A., Owens, T., Pawson, S., Pegion, P., Redder, C. R., Reichle, R., Robertson, F. R., Ruddick, A. G., Sienkiewicz, M., and Woollen, J.: MERRA: NASA's modern-era retrospective analysis for research and applications, J. Climate, 24, 3624–3648, 2011.

Rodgers, C. D.: Inverse Methods for Atmospheric Sounding: Theory and Practice, World Scientific, Singapore, 2000.

Schuh, A. E., Denning, A. S., Corbin, K. D., Baker, I. T., Uliasz, M., Parazoo, N., Andrews, A. E., and Worthy, D. E. J.: A regional high-resolution carbon flux inversion of North America for 2004, Biogeosciences, 7, 1625–1644, doi:10.5194/bg-7-1625-2010, 2010.

Skamarock, W. C. and Klemp, J. B.: A time-split nonhydrostatic atmospheric model for weather research and forecasting applications, J. Comp. Phys., 227, 3465–3485, 2008.

van der Werf, G. R., Randerson, J. T., Giglio, L., Collatz, G. J., Kasibhatla, P. S., and Arellano Jr., A. F.: Interannual variability in global biomass burning emissions from 1997 to 2004, Atmos. Chem. Phys., 6, 3423–3441, doi:10.5194/acp-6-3423-2006, 2006.

van der Werf, G. R., Randerson, J. T., Giglio, L., Collatz, G. J., Mu, M., Kasibhatla, P. S., Morton, D. C., DeFries, R. S., Jin, Y., and van Leeuwen, T. T.: Global fire emissions and the contribution of deforestation, savanna, forest, agricultural, and peat fires (1997–2009), Atmos. Chem. Phys., 10, 11707–11735, doi:10.5194/acp-10-11707-2010, 2010.

Wang, J. S., McElroy, M. B., Logan, J. A., Palmer, P. I., Chameides, W. L., Wang, Y., and Megretskaia, I. A.: A quantitative assessment of uncertainties affecting estimates of global

ACPD
14, 12819–12862, 2014

mean OH derived from methyl chloroform observations, J. Geophys. Res., 113, D12302, doi:10.1029/2007JD008496, 2008.

Yokota, T., Yoshida, Y., Eguchi, N., Ota, Y., Tanaka, T., Watanabe, H., and Maksyutov, S.: Global concentrations of CO_2 and CH_4 retrieved from GOSAT: first preliminary results, SOLA, 5, 160–163, doi:10.2151/sola.2009-041, 2009.

Zhao, C., Andrews, A. E., Bianco, L., Eluszkiewicz, J., Hirsch, A., MacDonald, C., Nehrkorn, T., and Fischer, M. L.: Atmospheric inverse estimates of methane emissions from Central California, J. Geophys. Res., 114, D16302, doi:10.1029/2008JD011671, 2009.

ACPD
14, 12819–12862, 2014

Table 1. Spatiotemporal correlation parameters used.

Month	Spatial correlation e-folding length (km)	Temporal correlation e-folding length (days)
Jan	481	17.2
Apr	419	7.2
Jul	284	6.9
Oct	638	1.6

ACPD
14, 12819–12862, 2014

Table 2. Flux uncertainties aggregated to entire continent and month or year (Pg C yr^{-1}).

	Jan	Apr	Jul	Oct	Annual
Standard inversion					
A priori	0.42	0.78	1.26	0.82	0.24
A posteriori (uncertainty reduction)					
Case 1	0.24 (43 %)	0.17 (78 %)	0.15 (88 %)	0.2 (76 %)	0.05 (78 %)
Case 2	0.33 (21 %)	0.28 (65 %)	0.26 (80 %)	0.31 (61 %)	0.08 (66 %)
Case 3	0.18 (57 %)	0.13 (83 %)	0.12 (91 %)	0.15 (81 %)	0.04 (83 %)
Case 4	0.28 (35 %)	0.22 (72 %)	0.2 (84 %)	0.25 (69 %)	0.07 (73 %)
Inversion with alternative correl. lengths (200 km, 35 days)					
A priori	0.23	0.59	1.27	0.59	0.21
A posteriori (uncertainty reduction)					
Case 1	0.17 (25 %)	0.15 (74 %)	0.14 (89 %)	0.16 (73 %)	0.04 (80 %)

ACPD
14, 12819–12862, 2014

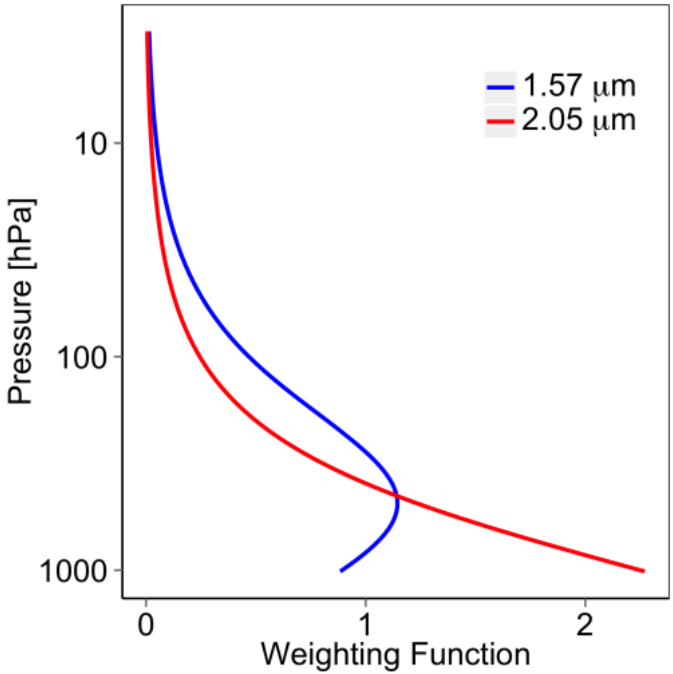

Figure 1. Vertical weighting functions (10^{-6} ppmv^{-1} h Pa^{-1}) for two candidate ASCENDS wavelengths. These relate differential optical depth lidar measurements (on-line minus off-line) to column-average CO_2 mixing ratios. The precise on-line wavelengths used here are 1.571121 μm, which is 10 picometers (pm) offset from line center, and 2.051034 μm.

ACPD
14, 12819–12862, 2014

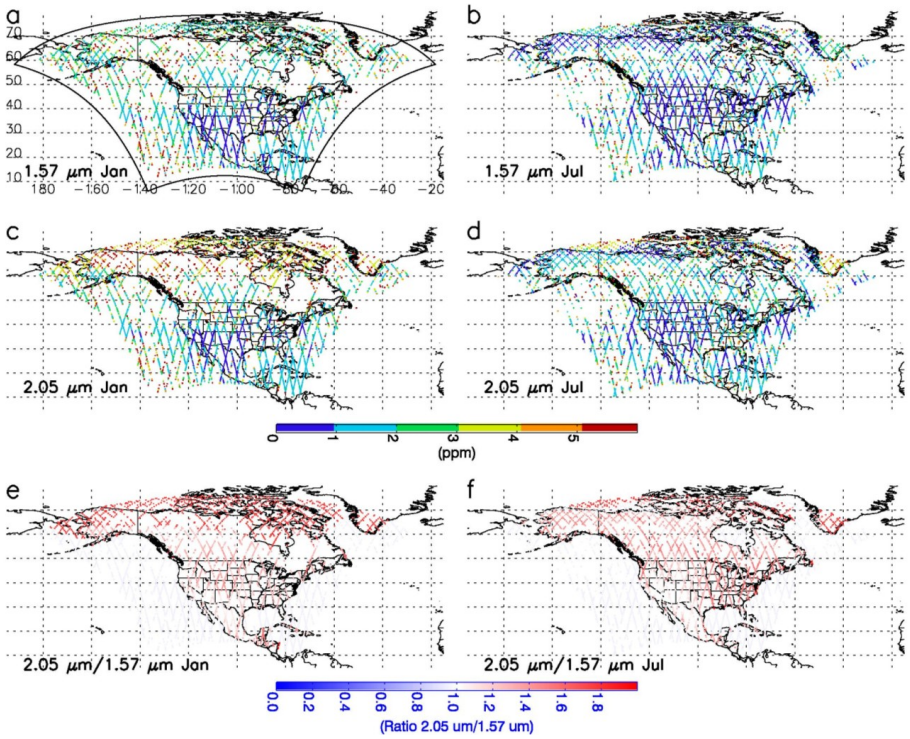

Figure 2. Examples of measurement locations (individual 10 s averages) and 10 s uncertainties (1σ) for the 0.5 ppm RRV random error case, across 7 day spans for **(a)** the 1.57 µm wavelength in January and **(b)** in July; and for **(c)** the 2.05 µm wavelength in January and **(d)** in July. Locations with OD > 0.7 are rejected. **(e)** Ratio of uncertainty for 2.05 µm to 1.57 µm in January and **(f)** in July. The WRF domain for the runs utilized in this study is indicated by the bold, black lines in **(a)**.

ACPD
14, 12819–12862, 2014

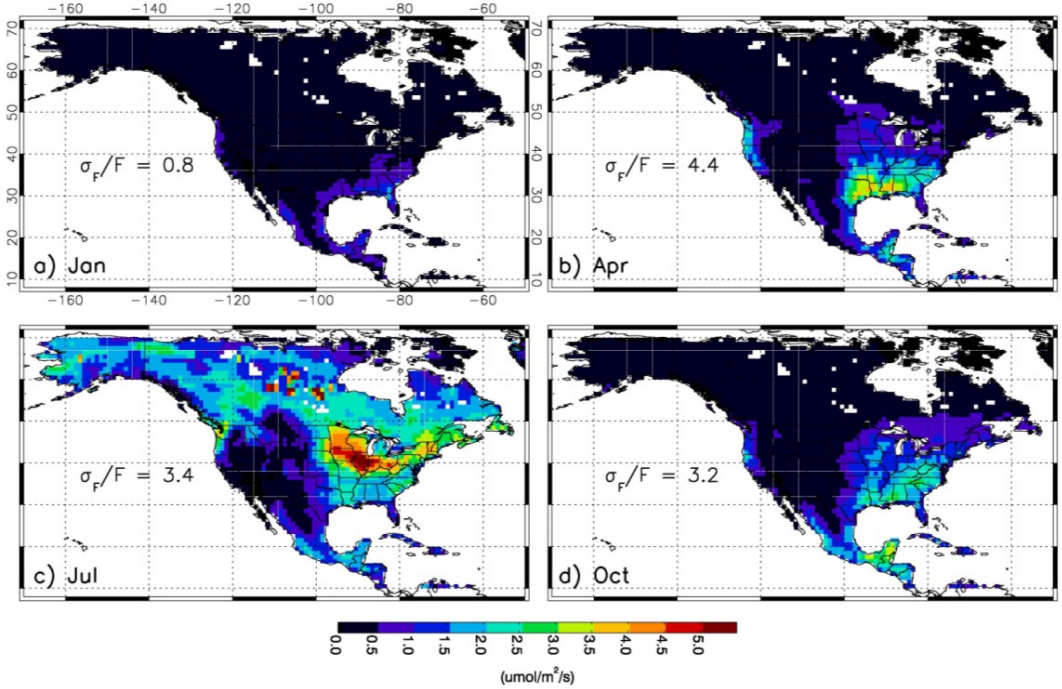

Figure 3. A priori weekly flux uncertainty for **(a)** January, **(b)** April, **(c)** July, and **(d)** October. Average fractional flux uncertainties over the domain are given in each panel. $1\,\mu mol\,m^{-2}\,s^{-1} = 1.037\,g\,C\,m^{-2}\,d^{-1} = 4.4 \times 10^{-8}\,kg\,CO_2\,m^{-2}\,s^{-1}$.

ACPD
14, 12819–12862, 2014

A regional CO_2 observing system simulation experiment

J. S. Wang et al.

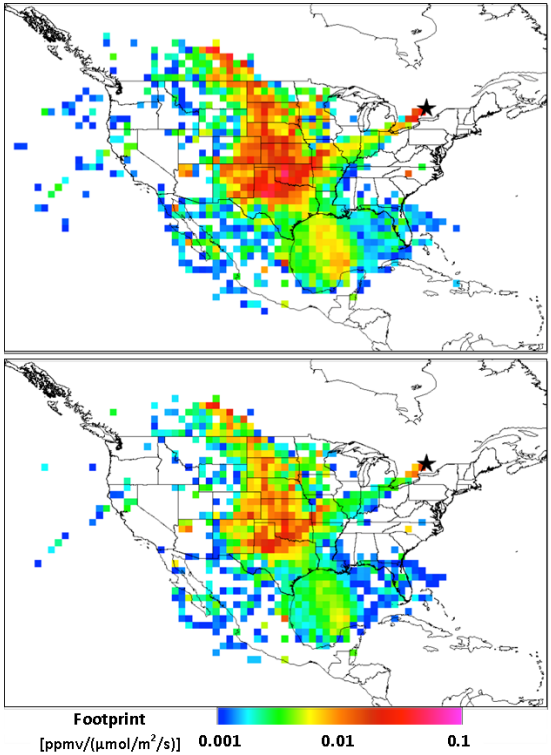

Figure 4. Footprint maps for one simulated ASCENDS measurement location (marked by black star) on 1 January 2007 at 18:00 UTC, integrated over 10 days and convolved over the 500–14 500 m a.g.l. range with two candidate ASCENDS weighting functions: for the CO_2 laser lines at 2.05 μm (top) and 1.57 μm (bottom). Units are ppm $(\mu mol\, m^{-2}\, s^{-1})^{-1}$. Note that the native temporal resolution of the footprints is 3 h; the 10 day integral in this figure is for illustrative purposes only. Only footprints over land are used in the analysis.

ACPD
14, 12819–12862, 2014

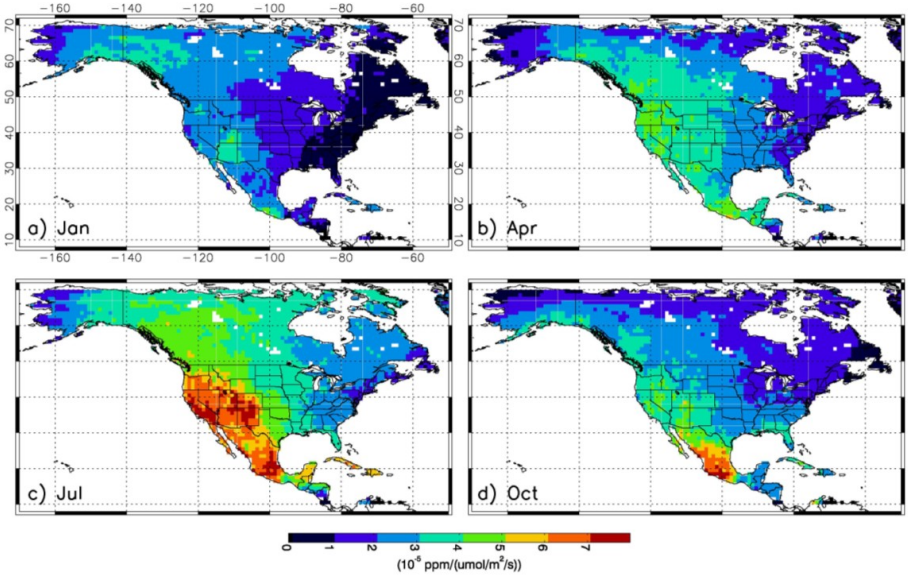

Figure 5. Jacobian values averaged over all observations and weekly flux intervals for **(a)** January, **(b)** April, **(c)** July, and **(d)** October, for the 1.57 µm weighting function.

ACPD
14, 12819–12862, 2014

A regional CO_2 observing system simulation experiment

J. S. Wang et al.

CC BY

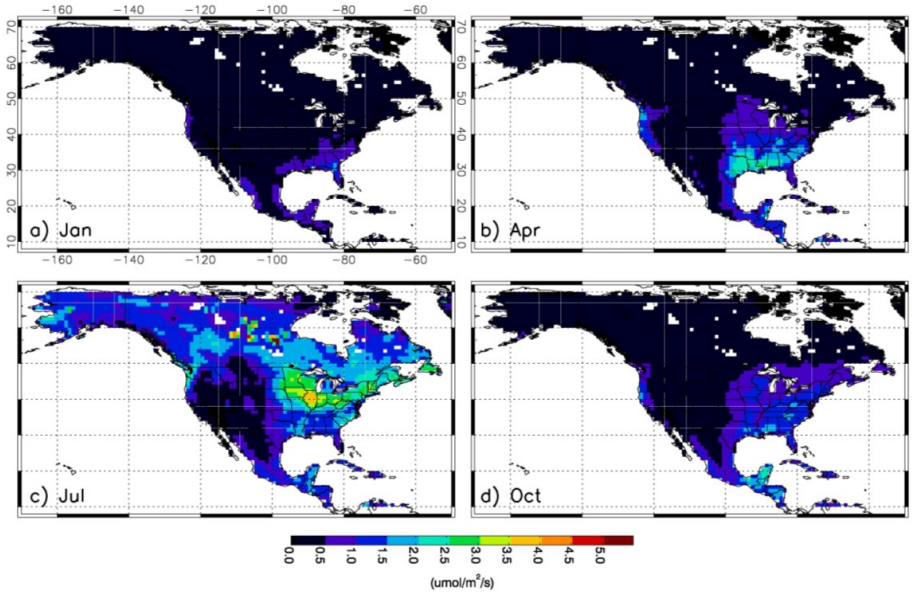

Figure 6. A posteriori weekly flux uncertainty over **(a)** January, **(b)** April, **(c)** July, and **(d)** October, for Case 1 (1.57 µm and 0.5 ppm RRV error). Shown here are RMS values from the first 4 weeks of each month. 1 µmol m^{-2} s^{-1} = 1.037 g C m^{-2} d^{-1} = 4.4×10^{-8} kg CO_2 m^{-2} s^{-1}.

ACPD
14, 12819–12862, 2014

A regional CO_2 observing system simulation experiment

J. S. Wang et al.

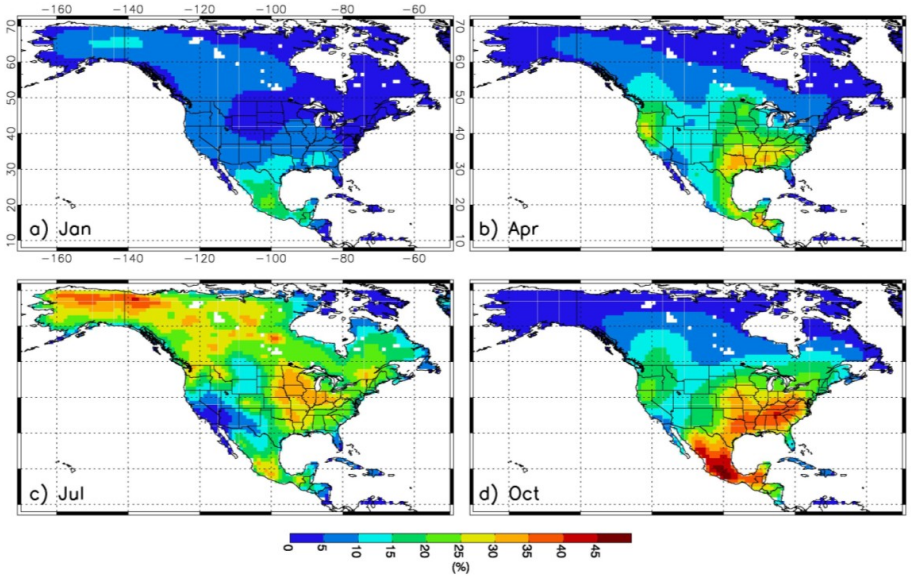

Figure 7. Weekly fractional flux uncertainty reduction over **(a)** January, **(b)** April, **(c)** July, and **(d)** October, for Case 1 (1.57 µm and 0.5 ppm RRV error). Shown here are results from the first 4 weeks of each month.

ACPD
14, 12819–12862, 2014

A regional CO_2 observing system simulation experiment

J. S. Wang et al.

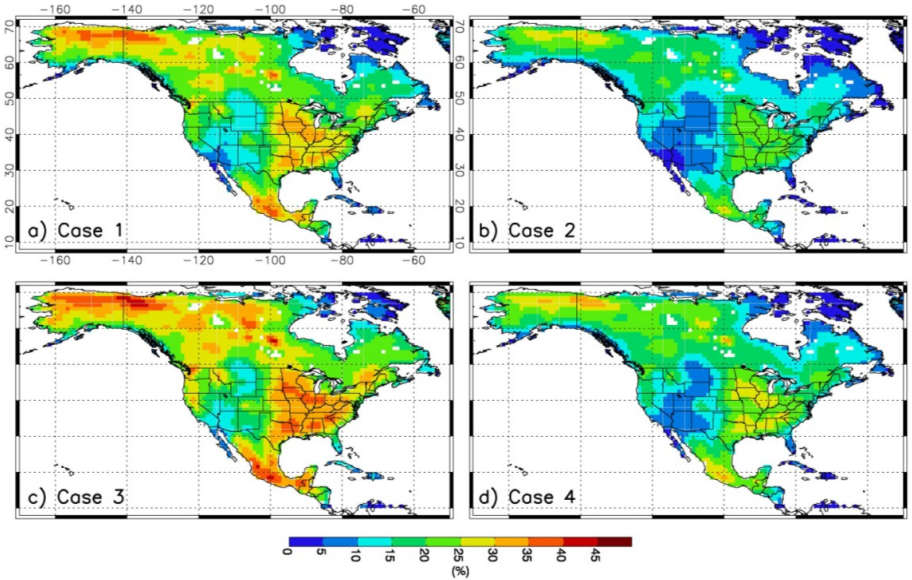

Figure 8. Weekly fractional flux uncertainty reduction (RMS over the 4 months) for **(a)** Case 1 (1.57 µm and 0.5 ppm RRV error), **(b)** Case 2 (1.57 µm and 1.0 ppm), **(c)** Case 3 (2.05 µm and 0.5 ppm), and **(d)** Case 4 (2.05 µm and 1.0 ppm).

ACPD
14, 12819–12862, 2014

A regional CO_2 observing system simulation experiment

J. S. Wang et al.

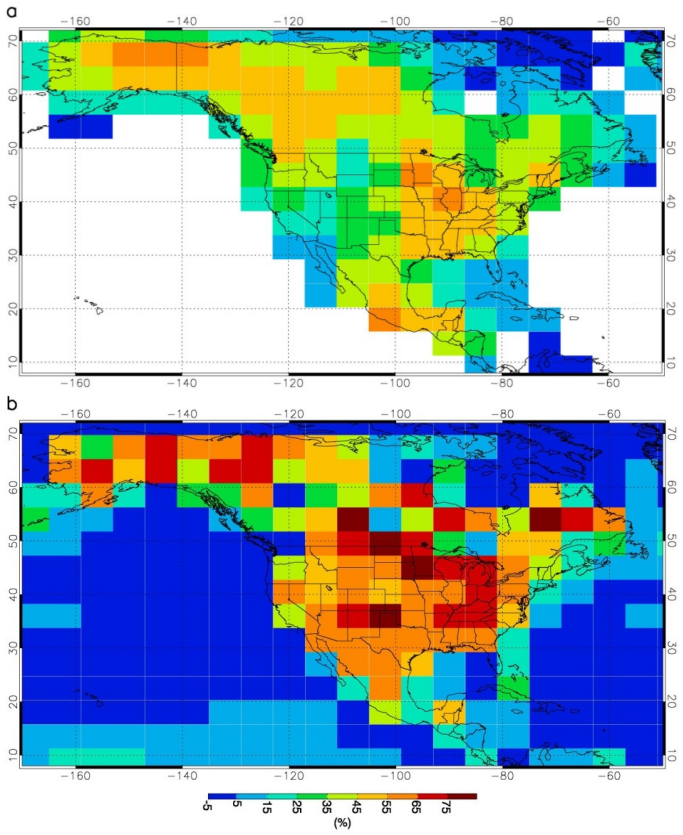

Figure 9. (a) Reduction in weekly flux uncertainty (RMS over 4 months) of the regional inversion, aggregated to 4.5° × 6° resolution, and **(b)** the global inversion results, which include ocean grid cells as well as land. Results in both panels are for the 1.57 µm wavelength and 0.5 ppm error case.

ACPD
14, 12819–12862, 2014

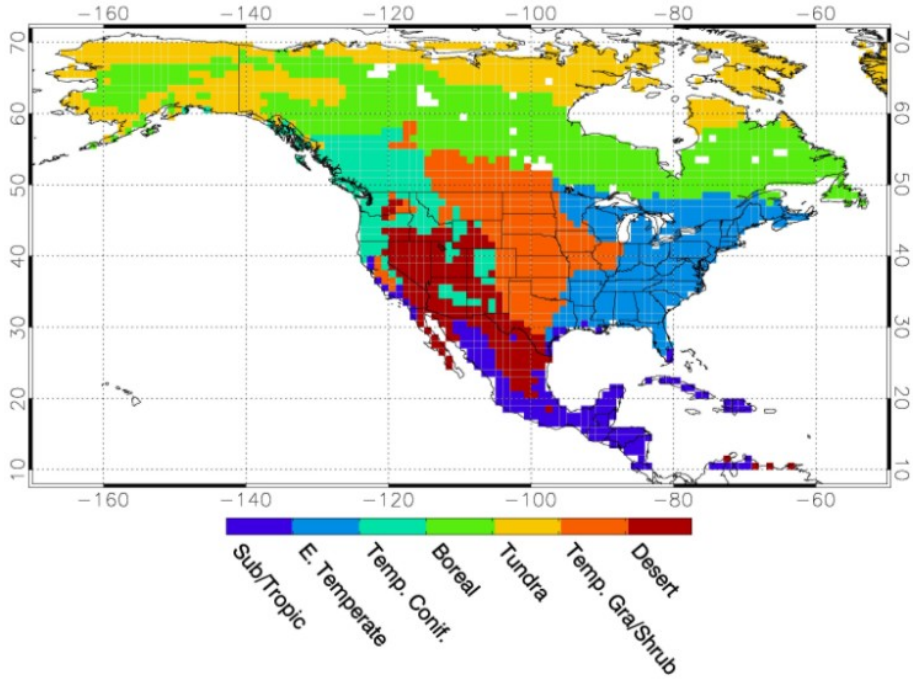

Figure 10. Biomes used, taken from Olson et al. (2001) with modifications by Gourdji et al. (2012).

ACPD
14, 12819–12862, 2014

A regional CO_2 observing system simulation experiment

J. S. Wang et al.

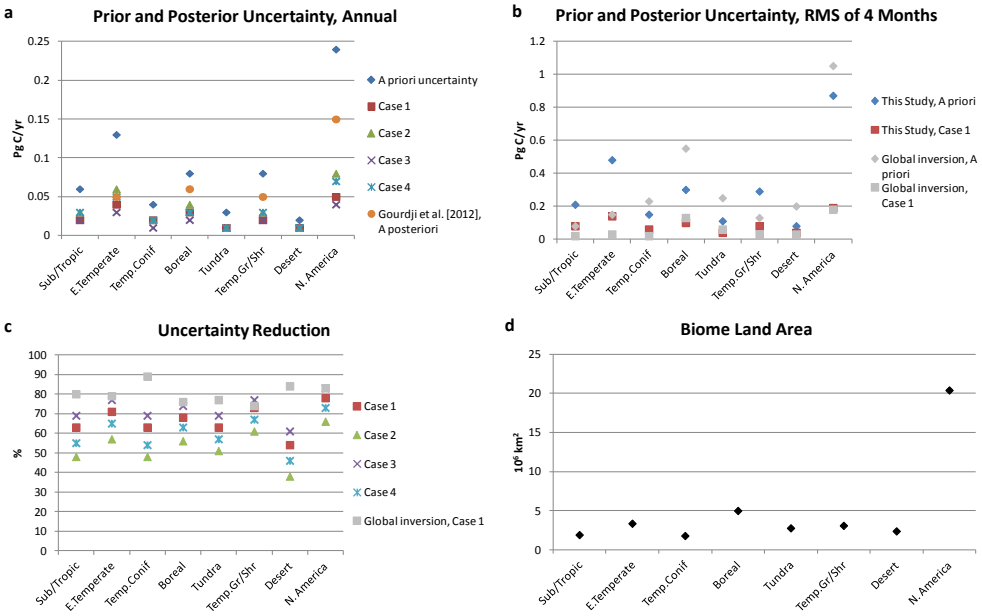

Figure 11. Results aggregated to biomes and continent, and compared with other studies. **(a)** A priori and a posteriori uncertainties for the year, including results from Gourdji et al. (2012). **(b)** RMS of the four monthly uncertainties, including results from the global inversion. **(c)** Fractional uncertainty reductions. **(d)** Land area of the biomes. Gourdji et al. reported results for only the three biomes that were well constrained by their in situ observation network, along with results aggregated over the full continent; we show the approximate average of their "Simple" and "NARR" inversions. The figure does not include a priori uncertainties for Gourdji et al. since their method does not rely on a priori estimates.

ACPD
14, 12819–12862, 2014

A regional CO_2 observing system simulation experiment

J. S. Wang et al.